



# Structural, Photoabsorption and Photocatalytic Characteristics of BiFeO<sub>3</sub>-WO<sub>3</sub> Nanocomposites: An Attempt to Validate the Experimental Data Through SVM-Based Artificial Intelligence (AI)

Yathavan Subramanian<sup>1</sup> · J. Gajendiran<sup>2</sup> · R. Veena<sup>1</sup> · Abul Kalam Azad<sup>1</sup> · V. C. Bharath Sabarish<sup>3</sup> · S. A. Muhammed Ali<sup>4</sup> · Avinash Kumar<sup>5</sup> · Ramesh Kumar Gubendiran<sup>3</sup>

Received: 27 September 2022 / Accepted: 19 December 2022 / Published online: 20 January 2023  
© The Minerals, Metals & Materials Society 2023

## Abstract

Nanocomposites of bismuth ferrite-tungsten trioxide (BiFeO<sub>3</sub>-WO<sub>3</sub>) were synthesized from sol–gel reaction followed by processing at two different calcination temperatures, 550°C and 650°C. The calcined composite products were investigated using powder XRD, FE-SEM, EDX, UV–Vis and FTIR to assess the influence of calcination temperature on their structural, morphological, and optical absorption properties and their photocatalytic characteristics. A photodegradation efficiency test was conducted for the synthesized BiFeO<sub>3</sub>-WO<sub>3</sub> nanocomposite powders, with methylene blue (MB) used as the dye source. The optimal experimental conditions required for the effective and maximized degradation of the MB pollutant were also determined, and the data authenticity was validated through an artificial intelligence (AI)-based support vector machine (SVM) tool. SVM predictions agreed reasonably well with the experimental results.

**Keywords** Nanocomposites · structural properties · optical absorption · photocatalysis · dye degradation · artificial intelligence · support vector machine (SVM) tool

## Introduction

Water contamination through industrial processes is a growing concern, as many organic dyes and medical wastes are discharged into water bodies. More specifically, dye processing and textile industries release several organic dye

pollutants, including methylene blue, azo-dye, and phenols, into water resources.<sup>1–3</sup> Among the industrial effluents, methylene blue dye is of specific interest as it has adverse effects on the reproductive and neural functions in both human beings and animals. It also poses a serious threat to human life and aquatic habitats. Hence, various pollution control boards have framed rules for the maximum allowable concentration of dye pollutants to be discharged into the water drainage upon treating industrial wastes.<sup>4,5</sup> To reduce the level of these kinds of contaminants from water resources, commercial water purification techniques have been used, but they are still not up to the mark due to their high input costs, high energy consumption and some environmental effects created by the chemicals used in them.<sup>6,7</sup> In addition, researchers are also facing great challenges in designing the photocatalysts with superior adsorption properties in degrading pharmaceutical effluents and dye molecules. To overcome the above disadvantages, various alternative approaches have been proposed, including advanced oxidation processes (AOP), Fe (VI) treatment technology, and adsorption and biological methods such as membrane processes, including microfiltration (MF), ultrafiltration (UF), nanofiltration (NF) and reverse osmosis (RO).<sup>8</sup> Among

✉ R. Veena  
veena.raj@ubd.edu.bn

✉ Ramesh Kumar Gubendiran  
rameshvandhai@gmail.com

<sup>1</sup> Faculty of Integrated Technologies, Universiti Brunei Darussalam, Gadong BE1410, Brunei

<sup>2</sup> Department of Physics, Vel Tech Rangarajan Dr, Sagunthala R&D Institute of Science and Technology, Avadi, Chennai 600 062, India

<sup>3</sup> Department of Science and Humanities, University College of Engineering Arni (Anna University), Arni, India

<sup>4</sup> Fuel Cell Institute, Universiti Kebangsaan Malaysia, 43600 Bangi, Selangor, Malaysia

<sup>5</sup> Department of Mechanical Engineering, Indian Institute of Information Technology, Design and Manufacturing, Kancheepuram, Chennai, India

these methods, the advanced oxidation process has gained significant interest due to the use of non-toxic, lower-cost and easily prepared photocatalytic materials. Materials commonly chosen for AOP should be capable of facilitating the generation of hydroxyl radicals required for oxidizing the dye molecules in wastewater.<sup>9,10</sup>

Among the photocatalytic materials, metal oxide-based semiconductors with a wide band gap such as TiO<sub>2</sub> and ZnO have been used for dye degradation using UV light. Dye degradation of TiO<sub>2</sub> material was first reported by Fujishima and Honda in 1972.<sup>11</sup> The prime disadvantages of wide band gap photocatalysts ( $E_g = 3\text{--}3.4$  eV) is that they cannot trap the visible portion of light and are responsive only to the UV regime.<sup>12</sup> In such instances, designing a visible light active photocatalyst having excellent stability with less recombination rate has become one of the challenges in photochemistry. Recently, perovskite oxide-based semiconductors have shown good performance in photocatalysis due to their excellent nature of light capturability and narrow band gap.<sup>13</sup> Bismuth ferrite (BiFeO<sub>3</sub>), in particular, is a material with optimum band gap (~2.0 eV) and good chemical stability.<sup>14–16</sup> This material is quite an attractive candidate for photocatalytic activity. However, its photocatalytic degradation efficiency seems to be limited due to the quick recoupling of photogenerated charge carriers. Therefore, heterogeneous photocatalysts are preferable, as they have a high separation rate for photogenerated electron–hole charge carriers and exhibit magnificent photocatalytic efficiency.

It may not be possible for any single semiconductor-based photocatalyst to meet all essential criteria such as visible light activeness, high stability and a lower rate of recombination. As an alternate option, new types of photocatalysts deduced by the way of coupling two or more semiconductors have recently been introduced and they were synthesized with the intention of improving their photocatalytic properties.<sup>17,18</sup> More specifically, tungsten oxide (WO<sub>3</sub>) is a unique metal oxide and it possesses characteristic electrical conductance and photocatalytic activity.<sup>19,20</sup> It also possess a narrow band gap of 2.4 eV. In addition, its non-toxicity, good stability, low density and lower cost have attracted researchers for its potential use in gas sensing elements, solar cells, and photocatalytic applications.<sup>21</sup> However, WO<sub>3</sub> exhibits lower photocatalytic characteristics because there are fewer active sites on its agglomerated surface. For instance, Mioduska et al.<sup>22</sup> reported on the synthesis of WO<sub>3</sub>/TiO<sub>2</sub>, wherein it was found that combining TiO<sub>2</sub> helped to improve the crystallinity of WO<sub>3</sub>, reduced the optical band gap and most importantly, decreased the agglomeration in the nanocomposite form. Therefore, WO<sub>3</sub> can be finely distributed with the low band gap semiconductor material. As such, combining with BiFeO<sub>3</sub> with WO<sub>3</sub> at different calcination temperatures of 550°C and 650°C is a viable option to extend the range of the visible light capture and to enhance the separation of the photogenerated electron–hole

carriers for the betterment of methylene blue dye degradation. Based on the literature survey, the adoption of the support vector machine (SVM) method to estimate MB dye removal using BiFeO<sub>3</sub>-WO<sub>3</sub> nanocomposite and optimization of process parameters at different temperatures has not been investigated elsewhere. Therefore, in the present work, we choose two different calcination temperatures, 550°C and 650°C, for the preparation of BiFeO<sub>3</sub>-WO<sub>3</sub> nanocomposites. We also proposed to determine its impact on their photocatalytic activity.

Further, photocatalytic degradation investigations carried out earlier on BiFeO<sub>3</sub>-WO<sub>3</sub> did not focus on the optimization of process parameters such as the pH of the reaction medium, the concentration of the pollutant and irradiation exposure time. These factors mainly determine the MB degradation efficiency. In our earlier work, BiFeO<sub>3</sub>-Bi<sub>2</sub>S<sub>3</sub> photocatalysts were identified with promising characteristics for the degradation of endocrine-disrupting compounds.<sup>23</sup> Therein, a complex non-linear relationship among the process parameters could be established and was also reflected in the outputs. Hence, it is strongly believed that the design of experiments and optimizing the process parameters would greatly reduce time and ambiguity. The modelling experiments use a novel artificial intelligence tool to help minimize the wastage of chemicals and also the experimental time. In order to predict the optimum process parameters for improving the degradation of dye molecules, an artificial intelligence-based support vector machine tool is preferred because the SVM tool consumes less time and is also cost-effective. It has also been extensively used in all fields of engineering and sciences.<sup>24,25</sup> In fact, support vector machine and artificial neural network (ANN) tools have already been adopted for predicting the degradation efficiency of Acid Red 73 using TiO<sub>2</sub> nanoparticles as the photocatalyst.<sup>26</sup> But none of them was found to have utilized the AI principles to validate the experimental dye degradation data and, therefore, it will be generally more beneficial to use AI to obtain reliable and authentic results. With this main objective, synthesis of BiFeO<sub>3</sub>-WO<sub>3</sub> at 550°C and 650°C has been proposed to remove the methylene blue dye pollutants and to evaluate the influence of calcination temperature on its structural, topographical and optical absorption properties. In addition, the interactive effects of the process parameters involved in the MB dye degradation were also analysed to determine the optimal conditions for achieving higher efficiency to degrade methylene blue dye using the SVM tool.

## Experimental Procedure

The starting materials used were of analytical grade (Merck, 99.9% Purity). Bismuth nitrate pentahydrate (Bi(NO<sub>3</sub>)<sub>3</sub>·5H<sub>2</sub>O), iron nitrate nonahydrate (Fe(NO<sub>3</sub>)<sub>3</sub>·9H<sub>2</sub>O), tungsten(VI) oxide (WO<sub>3</sub>), conc. nitric

acid (HNO<sub>3</sub>), tartaric acid (C<sub>4</sub>H<sub>6</sub>O<sub>6</sub>) and ethanol (C<sub>2</sub>H<sub>5</sub>OH) were the precursor chemicals. The synthesis procedure of BiFeO<sub>3</sub>-WO<sub>3</sub> nanocomposites, as appended in our reported work<sup>27</sup> at 500°C, has now been repeated at different calcination temperature, 550°C and 650°C.

## Material Characterization

Powder XRD patterns of the synthesized nanocomposites were recorded using a PANalytical X'Pert PRO x-ray diffractometer with CuK $\alpha$  radiation of wavelength  $\lambda = 1.54056 \text{ \AA}$ . An FE-SEM (Carl Zeiss) attached to an EDX analyser was utilized to determine the quantitative presence of elements and the topographical features of the synthesized composite samples. Optical absorption measurements were done in the wavelength range 200 to 800 nm using a UV-2450 SHIMADZU spectrophotometer. In order to study the vibrational structure of the composite sample, FT-IR spectra have been recorded at room temperature in the frequency range 400–4000 cm<sup>-1</sup> using a Shimadzu IR Affinity-1 spectrophotometer.

## Photodegradation Test

Optical absorption of the photocatalyst has been recorded using a LAB INDIA double beam UV-Vis spectrophotometer. Ten milligrams of synthesized composite (as a photocatalyst) and 10 mL of methylene blue dye (10 mg/L) were dispersed in the aqueous solution containing the photocatalyst. The solution was then stirred under dark conditions for 120 min to ensure equilibrium between adsorption and desorption. Upon attaining equilibrium, the MB composite solution mixture was kept under natural sunlight. At every 3-h interval, 4-mL aliquots were pipetted out of the glass tube and centrifuged to prepare the solution for degradation analysis.

## Powder XRD Analysis on BiFeO<sub>3</sub>-WO<sub>3</sub> Nanocomposites

Diffraction patterns recorded in the  $2\theta$  range 20°–60° at a scan rate of 2°/min for the synthesized BFO-WO<sub>3</sub> composites calcined at 550°C and 650°C are shown in Fig. 1. The diffracted peak positions for the obtained composite samples have been compared with the standard JCPDS files of BiFeO<sub>3</sub> and WO<sub>3</sub>.<sup>27</sup> All peaks with moderate intensities were correctly indexed to their corresponding (hkl) planes, confirming the presence of the rhombohedral phase of BiFeO<sub>3</sub> as well as the monoclinic nature of WO<sub>3</sub>. The mixed crystalline phases as evidenced from XRD would authenticate the formation of BFO-WO<sub>3</sub> nanocomposites. With increasing calcination temperature from 550°C to 650°C, the diffraction peaks sharpened, indicating improvement in the degree

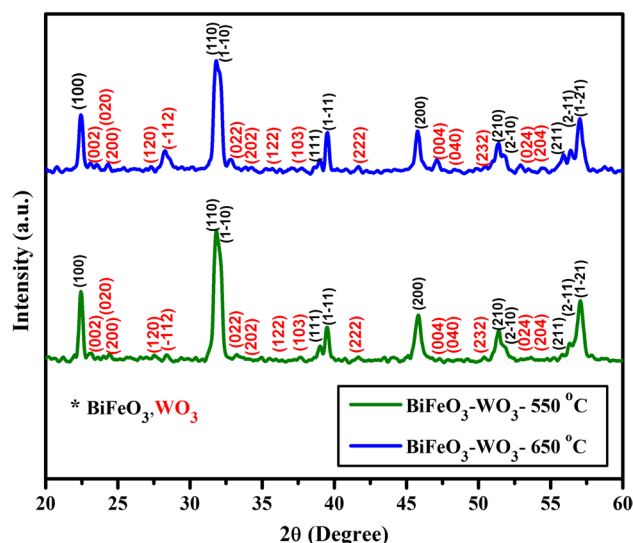


Fig. 1 XRD patterns of BiFeO<sub>3</sub>-WO<sub>3</sub> nanocomposites calcined at 550°C and 650°C

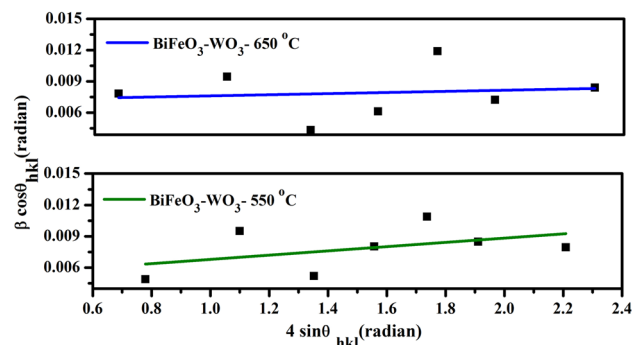


Fig. 2 W–H plots for BiFeO<sub>3</sub>-WO<sub>3</sub> nanocomposites synthesized at 550°C and 650°C

of crystallinity and structural coarsening. In addition, the particle sizes increased, which could be perceived from peak broadening, as expected.

In order to assess the crystalline strain and size, Williamson-Hall (W–H) analysis<sup>28</sup> was done for the calcined samples of BiFeO<sub>3</sub>-WO<sub>3</sub> samples. Using the computed trigonometric values of  $4\sin\theta$  and  $\beta\cos\theta$ , linear fits were obtained for the composite powders calcined at 550°C and 650°C and are shown in Fig. 2. Crystallite size and induced strain were calculated for the BiFeO<sub>3</sub>-WO<sub>3</sub> composites calcined at 550°C and 650°C as per the following equation.

$$\beta_{hkl} = [(\beta_{hkl})_{\text{measured}}^2 - (\beta_{hkl})_{\text{instrumental}}^2]^{1/2} \quad (1)$$

$$D = \left( \frac{K\lambda}{\beta_{(hkl)} \cos\theta} \right) \quad (2)$$

$$\varepsilon = \left( \frac{\beta_{(hkl)}}{4 \tan \theta} \right) \quad (3)$$

$$\beta_{(hkl)} = \left( \frac{K\lambda}{D \cos \theta} \right) + 4\varepsilon \sin \theta, \quad (4)$$

$$\beta_{(hkl)} \cos \theta = \left( \frac{K\lambda}{D} \right) + 4\varepsilon \sin \theta, \quad (5)$$

where  $D$  is the crystallite size,  $K$  is the shape factor (0.94),  $\lambda$  is the wavelength of  $\text{CuK}\alpha$  radiation,  $\theta$  is the Bragg angle,  $\beta_{hkl}$  is the full width at half maximum, and  $\varepsilon$  is the crystalline strain.

Table I indicates an increased crystallite size and decreased induced strain for the composite calcined at  $650^\circ\text{C}$  when compared to the composite calcined at  $550^\circ\text{C}$ . This may be due to the decrease in crystalline defects. Consequently, its crystallinity appears to have improved.

### FE-SEM Analysis of $\text{BiFeO}_3\text{-WO}_3$ Nanocomposites

Particle growth and surface morphology are considered to be key factors affecting photocatalytic activity. Therefore, topographical features of  $\text{BiFeO}_3\text{-WO}_3$  nanocomposites calcined at  $550^\circ\text{C}$  and  $650^\circ\text{C}$  were analysed through FE-SEM images, and they are shown in Fig. 3a and b. In the case of  $\text{BiFeO}_3\text{-WO}_3$  nanocomposites calcined at  $550^\circ\text{C}$ , the sample surface was found to be distributed with  $\text{BiFeO}_3$  spherical-shaped particles and  $\text{WO}_3$  appeared to be plate-like particles, as indicated by arrows in FE-SEM images. From Fig. 3b, the 2D structure of the  $\text{BiFeO}_3\text{-WO}_3$  calcined at  $650^\circ\text{C}$  can be found with increased grain growth and surface is also more agglomerated when compared to the sample calcined at  $550^\circ\text{C}$ . The increase in temperature makes the composite powders coarser and more agglomerated and in turn may decrease the surface area. This is likely to influence its physical properties. Cai et al.<sup>29</sup> observed that the higher calcination temperature of  $600^\circ\text{C}$  for Mn-C-codoped  $\text{TiO}_2$  had strong effects on the photocatalytic properties. Hence, upon increasing the calcination temperature, the surface morphology of the  $\text{BiFeO}_3\text{-WO}_3$  nanocomposites show a shrinking in surface area, growth of crystallite size and also enhanced agglomeration, resulting in a decrease in the photocatalytic activity. These changes in the morphological features of

**Table I** Crystalline strain and sizes of  $\text{BiFeO}_3\text{-WO}_3$  nanocomposites

S. No.	Sample code	Calcination temperature, $^\circ\text{C}$	Crystalline Size, nm	Strain (unitless)
1	$\text{BiFeO}_3\text{-WO}_3$	550	~ 36 nm	$6.9 \times 10^{-2}$
2		650	~ 40 nm	$3.7 \times 10^{-2}$

$\text{BiFeO}_3\text{-WO}_3$  would drastically modify their photocatalytic behaviour. Energy-dispersive x-ray (EDX) patterns, as shown in Fig. 3c and d, depict the percentage composition of Bi, W, Fe, and O present in the synthesized composites calcined at  $550^\circ\text{C}$  and  $650^\circ\text{C}$ . The chemical compositions of the individual elements in the as-synthesized nanocomposites did not show much variation with the increase in calcination temperature. However, the measurement clearly substantiates that both bismuth ferrite and tungsten oxide molecules are non-uniformly distributed throughout the composite system.

### UV-Vis-NIR Studies of $\text{BiFeO}_3\text{-WO}_3$ Nanocomposites

Photoabsorption properties of  $\text{BiFeO}_3\text{-WO}_3$  composite samples calcined at  $550^\circ\text{C}$  and  $650^\circ\text{C}$  were analysed using the UV-Vis-NIR spectra and are shown in Fig. 4a and b. By observing the graphs, it is noticed that compared with the  $\text{BiFeO}_3\text{-WO}_3$  composite sample calcined at  $550^\circ\text{C}$ , the composite sample calcined at  $650^\circ\text{C}$  shows a significant change in the optical absorption, and  $\lambda_{\text{max}}$  appears to be shifting towards a longer wavelength side, indicating a redshift due to the increased crystallite size upon the increase in calcination temperature. The band gap energies ( $E_g$ ) have been computed using the Kubelka-Munk (KM) function<sup>30</sup> and Tauc plots have been drawn and are given in Fig. 4b. The obtained  $E_g$  value of the  $\text{BiFeO}_3\text{-WO}_3$  nanocomposite calcined at  $650^\circ\text{C}$  (1.98 eV) was found to be relatively smaller than that of  $\text{BiFeO}_3\text{-WO}_3$  calcined  $550^\circ\text{C}$  (2.0 eV). The decrease in  $E_g$  from 2.0 eV to 1.98 eV increased the sample's optical absorption in the visible region. Therefore, it can be concluded that temperature variation likely aids in tuning the band gap energy and in turn may influence the photocatalytic activity.<sup>29</sup> In addition, the band gap value of bare  $\text{BiFeO}_3$  was reported in an earlier work as ~ 1.8 eV,<sup>27</sup> and the bare  $\text{WO}_3$ , which was purchased commercially, has a band gap value of 2.4 eV.

### Vibrational Analysis of $\text{BiFeO}_3\text{-WO}_3$ Nanocomposites

FT-IR spectra recorded in the frequency range  $400\text{--}1000\text{ cm}^{-1}$  on  $\text{BiFeO}_3\text{-WO}_3$  composites calcined at  $550^\circ\text{C}$  and  $650^\circ\text{C}$  are represented in Fig. 5. A broad IR absorption noticed in the region of  $400\text{--}700\text{ cm}^{-1}$  for both calcined composite samples corresponds to the interaction binding between Bi-O, Fe-O, and W-O. This specific absorption perhaps indicates the formation bismuth ferrite with tungsten oxide as a nanocomposite.<sup>31,32</sup> Further, this broad IR band is also slightly shifted towards the low-frequency side for the nanocomposite samples calcined at  $650^\circ\text{C}$ .

Based on the above observation, it is clear that the calcination temperature has once again played a key role in the optical absorption properties even in the IR regime. In the



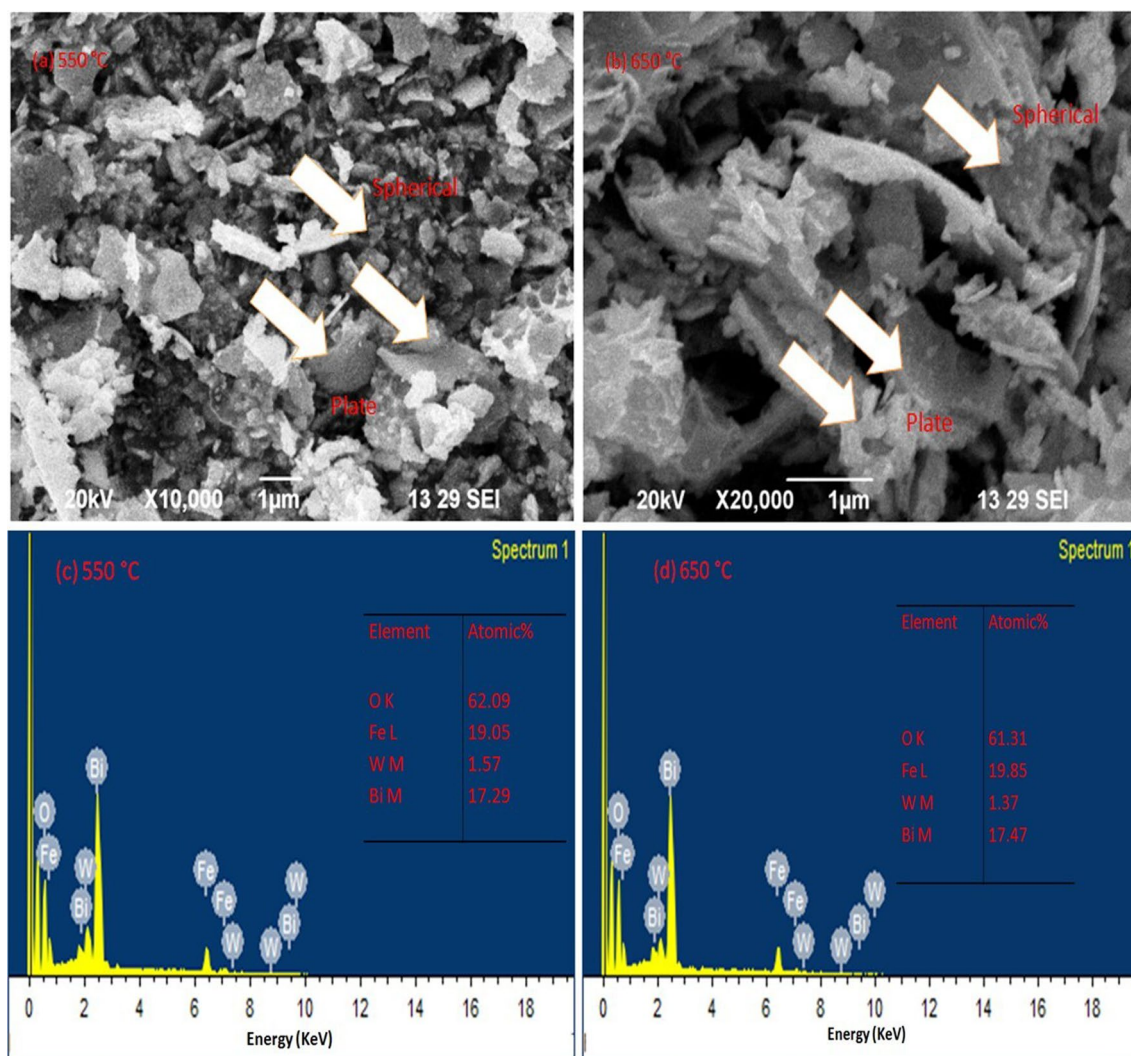


**Fig. 3** Distribution of particles in BiFeO<sub>3</sub> and WO<sub>3</sub> through FE-SEM for composite samples calcined at (a) 550 °C and (b) 650 °C; (c) and (d) EDX patterns, which indicate the percentage composition of each element present in the sample.

frequency interval 700–4000 cm<sup>-1</sup> (shown as an inset in Fig. 5), no additional functional groups are seen other than BiFeO<sub>3</sub>-WO<sub>3</sub>, so it can be concluded that the synthesized composites contained only the expected crystalline phases without any additional impurities.

### Photocatalytic Dye Degradation Activity of BiFeO<sub>3</sub>-WO<sub>3</sub> Composites

In order to study the photocatalytic behaviour, synthesized composites have been utilized as photocatalysts, and methylene blue (MB) was used as an industrial effluent. Degradation experiments were performed under natural sunlight illumination on the synthesized BiFeO<sub>3</sub>-WO<sub>3</sub> composite in the presence of known concentrations of MB dye solution. A few milliliters of degraded dye solution was taken every 3 h and the absorption spectra were also recorded at regular

intervals of time. The obtained spectra are shown in Fig. 6a and b. The rate of dye degradation with respect to exposure time and degradation efficiencies for various illumination periods have been computed and are presented in Fig. 6c and d.

While observing the photodegradation activity of MB dye/BiFeO<sub>3</sub>-WO<sub>3</sub> photocatalyst solution, the maximum absorbance peak appearing initially at 652 nm was found to gradually decrease with increasing time of irradiance. Dye degradation efficiency was thus estimated from the decrease in the absorbance rate through UV–visible spectra, and efficiencies are given in Table II.

From the above table, it is inferred that an increase in calcination temperature likely causes a decrease in the photodegradation efficiency, and this implies the influence of surface morphological features and crystallite sizes on the photocatalytic behaviour of the composite used for study. As

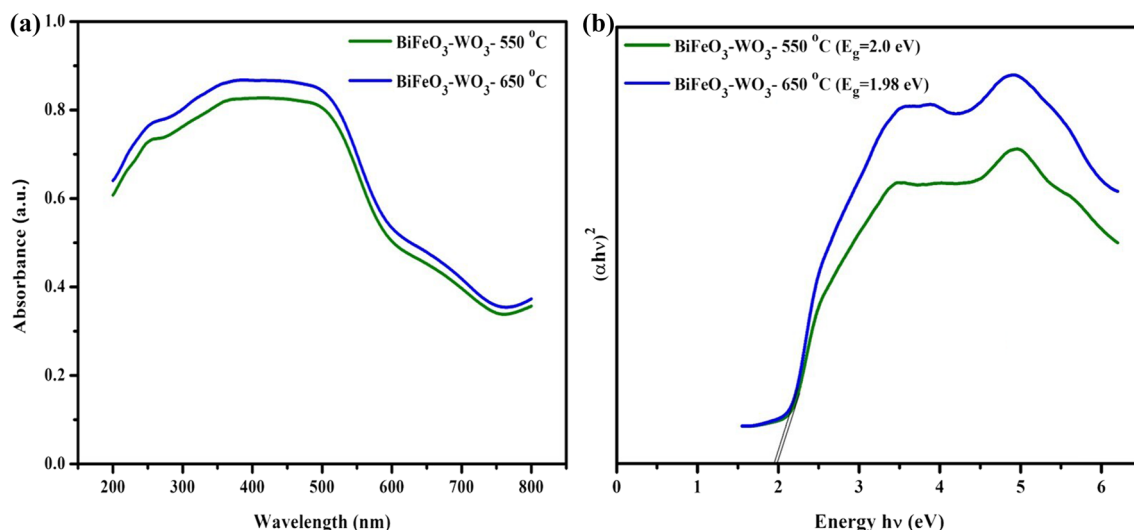


**Fig. 4** (a) UV-Vis spectra of BiFeO<sub>3</sub>-WO<sub>3</sub> nanocomposites calcined at 550°C and 650°C and (b) Tauc plots drawn for the same set of samples.

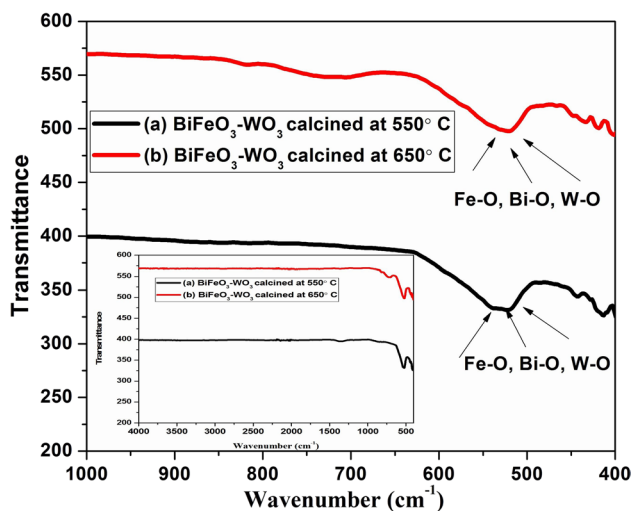


**Fig. 5** FT-IR spectra of BiFeO<sub>3</sub>-WO<sub>3</sub> composites calcined at (a) 550°C and (b) 650°C.

a consequence, visible light seems to be much more active for a good surface area with smaller particles. They possess good contact with dye molecules and also produce low chances of recombination of charge carriers. Low MB dye degradation for the BiFeO<sub>3</sub>-WO<sub>3</sub> sample calcined at 650°C was observed due to its increased particle sizes and because of its more agglomerated characteristics. Accordingly, the surface contact of the photocatalyst with dye molecules decreases and leads to the incomplete decomposition of methylene blue. The methylene blue degradation efficiencies have been calculated for the synthesized composite samples calcined at 550°C and 650°C using an efficiency formula adopted elsewhere<sup>33</sup> and confirm that the sample calcined

at 550°C exhibited better photocatalytic properties over that calcined at 650°C.

The possible mechanism for the photocatalytic degradation of methylene blue dye using the nanocomposite of BiFeO<sub>3</sub>-WO<sub>3</sub> calcined at 550°C is shown in Fig. 7. To hypothesize the process of photocatalytic degradation of methylene blue dye using BiFeO<sub>3</sub>-WO<sub>3</sub> photocatalysts, the locations of the valence band (VB) and conduction band (CB) edges of BiFeO<sub>3</sub> and WO<sub>3</sub> semiconductors must be determined using the Mullikan electronegativity approach<sup>34,35</sup> by following steps 1 and 2 as follows.

Step 1: Compute the conduction band positions ( $E_{CB}$ ) of BiFeO<sub>3</sub> and WO<sub>3</sub> semiconductors using the relation

$$E_{CB} = X - 4.5 (E_e) - E_g/2 \quad (6)$$

where  $X$  is the electronegativity value of the BiFeO<sub>3</sub> and WO<sub>3</sub> semiconductors;  $E_e$  is the energy of a free electron on a hydrogen scale (4.5 eV); and  $E_g$  is the band gap energy value of the BiFeO<sub>3</sub> (~1.8 eV) and WO<sub>3</sub> (~2.4 eV) semiconductors.

Step 2: Using  $E_{CB}$  and  $E_g$  values, compute the value of valence band positions ( $E_{VB}$ ; with respect to the standard hydrogen electrode) of BiFeO<sub>3</sub> and WO<sub>3</sub> using the formula

$$E_{VB} = E_{CB} + E_g \quad (7)$$

Based on this, the conduction band potentials of BiFeO<sub>3</sub> and WO<sub>3</sub> were computed as 0.4 eV and 0.8 eV, and their valence band potentials were found to be 2.2 eV and 3.2 eV, respectively. These band gap edges are incredibly beneficial for developing a unique heterojunction system between the p-type BiFeO<sub>3</sub> and n-type WO<sub>3</sub> during interface. Prior to contact, the Fermi energy level of p-type BiFeO<sub>3</sub> and

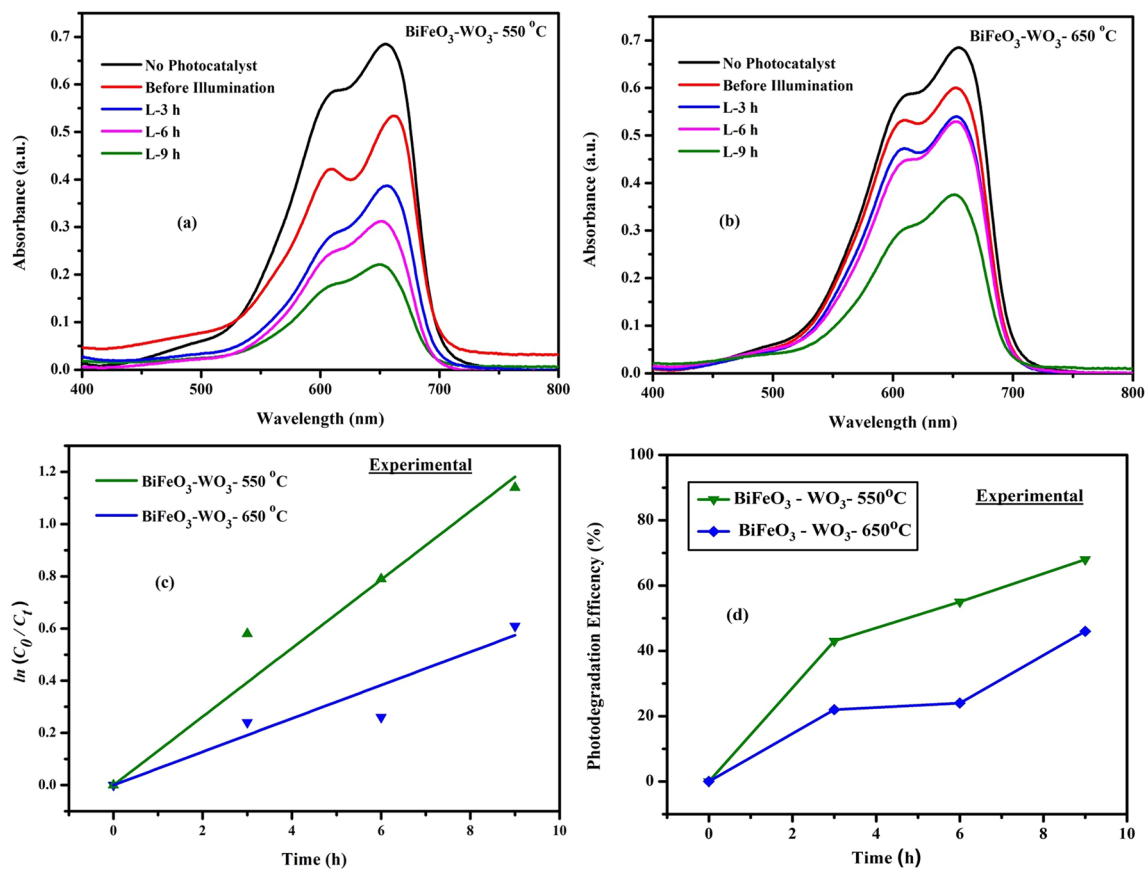


**Fig. 6** (a) and (b) Experimentally obtained photodegradation response of the BiFeO<sub>3</sub>-WO<sub>3</sub> composites to the MB dye, (c) Exposure time versus  $\ln(C_0/C_t)$ , (d) Photodegradation efficiencies for the BiFeO<sub>3</sub>-WO<sub>3</sub> nanocomposites calcined at 550°C and 650°C.

n-type WO<sub>3</sub> are close to their valence band. After making contact, the Fermi energy levels move towards each other,

excited to its conduction band and then transferred to the conduction band of WO<sub>3</sub> because of the CB offset. At the

**Table II** Experimentally obtained MB degradation pseudo first-order kinetics and degradation efficiency for the BiFeO<sub>3</sub>-WO<sub>3</sub> nanocomposites calcined at 550°C and 650°C

S. No.	Sample code	Temperature (°C)	Pseudo first-order kinetics			Methylene blue degradation efficiency (%)		
			Slope k (min <sup>-1</sup> )	Standard Error	R <sup>2</sup> value	3 h	6 h	9 h
1	BiFeO <sub>3</sub> - WO <sub>3</sub>	550	0.131(1)	0.009(6)	0.978(9)	43	55	69
2		650	0.063(8)	0.006(7)	0.956(3)	22	24	46

and the movement of photogenerated charge carriers occurs at the p-type BiFeO<sub>3</sub> and n-type WO<sub>3</sub> hetero-interface. This resulted in the formation of an internal electric field, which might provide a potent driving force for easing the process of electron transfer and segregation.<sup>36–38</sup> Upon illumination with natural sunlight, the photogenerated charge carriers, such as electron (e<sup>-</sup>) and holes (h<sup>+</sup>) pairs, are produced inside the BiFeO<sub>3</sub>-WO<sub>3</sub> nanocomposite. Initially, the photogenerated electrons in the valence band of BiFeO<sub>3</sub> are

same time, the holes on the valence band of the WO<sub>3</sub> moved to the valence band of BiFeO<sub>3</sub> due to the VB offset. Then these charge carriers migrate onto the photocatalyst surface to take part in subsequent photocatalytic reactions. The electrons in the CB of WO<sub>3</sub> generate superoxide radicals ( $\cdot\text{O}_2^-$ ) by reacting with molecular oxygen in the reaction chamber. Then  $\cdot\text{O}_2^-$  reacts with water molecules to create hydroxyl ( $\cdot\text{OH}$ ) radicals. Similarly, photoinduced holes in the VB of BiFeO<sub>3</sub> oxidize water molecules to produce  $\cdot\text{OH}$  radicals.

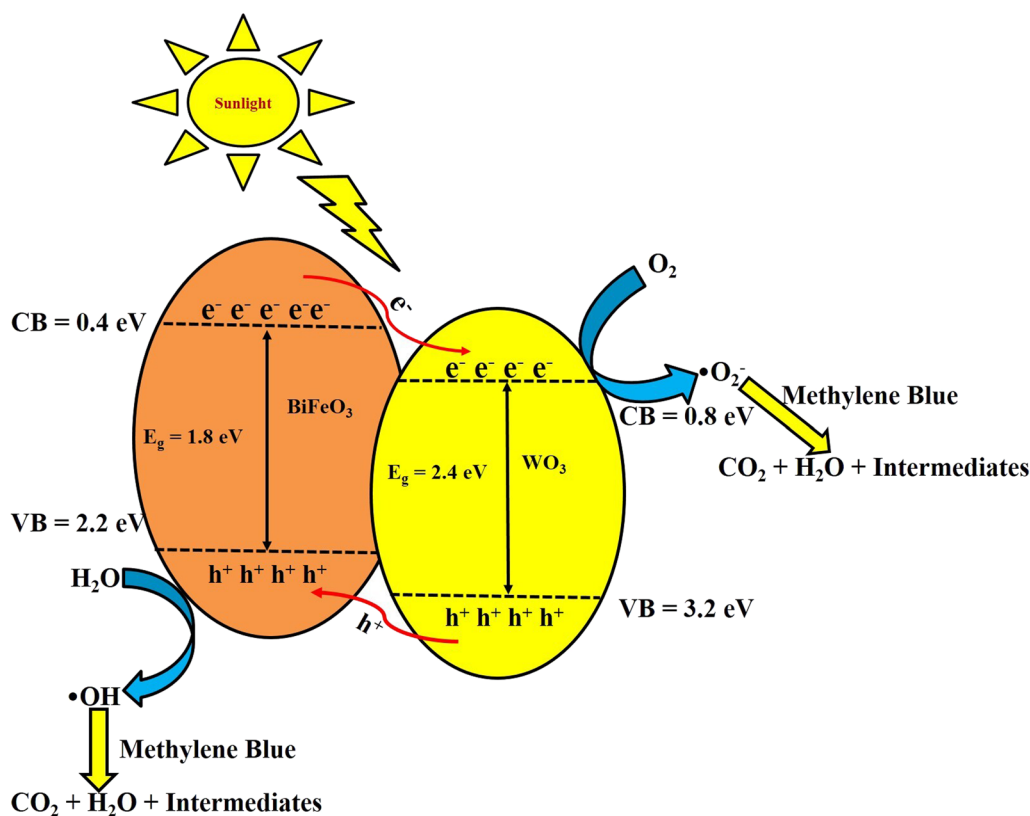


Fig. 7 Proposed photocatalytic mechanism for BiFeO<sub>3</sub>-WO<sub>3</sub> nanocomposites.

These hydroxyl and superoxide radicals react with the methylene blue dye adsorbed on the photocatalyst surface to degrade into carbon dioxide and water molecules upon sunlight illumination. In addition, higher MB degradation efficiency of BiFeO<sub>3</sub>-WO<sub>3</sub> calcined at 550°C was also strongly dependent on parameters such as calcination temperature, surface morphological features and crystallite sizes. They also play a vital role in generating  $\cdot\text{O}_2^-$  and  $\cdot\text{OH}$  species, which supports enhancement of the photocatalytic characteristics of the BiFeO<sub>3</sub>-WO<sub>3</sub> nanocomposites. In summary, the higher MB degradation behaviour of the BiFeO<sub>3</sub>-WO<sub>3</sub> calcined at 550°C was observed with the combined influence of wider surface area, narrower band gap, effective charge transfer kinetics, and formation of built-in electric field at the BiFeO<sub>3</sub> and WO<sub>3</sub> interface.

### SVM Computation of Dye Degradation Rate and Efficiencies

The support vector machine is a traditional machine learning approach that can be utilized for classification and regression applications. SVM augments fundamental machine learning algorithms with features that make them more effective in a variety of applications.<sup>39,40</sup> The support vector machine tool was first introduced by Oyehan et al.<sup>41</sup> and it is a robust

machine learning technique that can be used to model and validate the complex non-linear relationship between process variables and their outputs.<sup>42</sup> The SVM tool has been applied here to validate the experimental data used for the removal of MB dye in aqueous solution using four operational variables, which are termed as the estimators. The input parameters such as pH, dye concentration, photocatalyst dose and irradiation exposure time were provided to run the SVM algorithm and are tabulated in Table III.

The inputs of MB degradation models are randomly divided into two subsets used: 85% for training and 15% for testing. Dye degradation efficiency [DDE (%)] and rate constant performance ( $R^2$ ) for the synthesized samples were predicted and compared with the experimental results. The predicted result is useful to analyse the influence of MB dye degradation process parameters and to find the optimal conditions for obtaining the higher rate of methylene blue degradation. In order to evaluate through SVM, two formulae are used for the measuring the rate constant performance ( $R^2$ ) and DDE (%) are shown as the Eqs. 8 and 9.

$$R^2 = 1 - \frac{\sum_{i=1}^N (E_{pred,i} - E_{exp,i})^2}{\sum_{i=1}^N (E_{pred,i} - \bar{E}_{exp,i})^2} \quad (8)$$



$$\%DDE = \frac{100}{N} \sum_{i=1}^N \left| \frac{E_{pred,i} - E_{exp,i}}{E_{exp,i}} \right| \quad (9)$$

Figure 8a shows the SVM-generated values of MB dye degradation efficiencies for the photocatalyst samples calcined at 550°C and 650°C. According to the SVM prediction, the optimal condition for maximum methylene blue degradation efficiency of 67% was obtained from BiFeO<sub>3</sub>-WO<sub>3</sub> composite synthesized at the calcination temperature of 550°C with an irradiation time of 9 h, whereas for the same exposure time, the degradation efficiency of BiFeO<sub>3</sub>-WO<sub>3</sub> composite synthesized at 650°C was predicted as 49.5%. This shows the excellent agreement between predicted and experimental degradation values, confirming that SVM can be used as a tool for validating the MB dye degradation experimental results. The results of R<sup>2</sup> obtained experimental data fit have also been compared with SVM

**Table III** List of input variables along with the measurement range of the input and output parameters

S. No.	Operational variables	Measurement range	Input/Output
1	Irradiation time (h)	0–9	Input
2	Concentration of methylene blue (mg/L)	5–10	Input
3	Photocatalyst dosage (mg/L)	5–10	Input
4	pH of the medium	5–6	Input
5	Methylene blue removal rate (%)	0–100	Output

prediction and are tabulated in Table IV.

From Fig. 8b, it has been found that the R<sup>2</sup> values obtained through SVM for the BiFeO<sub>3</sub>-WO<sub>3</sub> composite calcined at 550°C are reasonably appropriate with the experimental fit, indicating that the present tool is a good kinetic model. The SVM tool can also produce excellent fits with the experimental results in a shorter time, and obtained R<sup>2</sup> values are nearly unity. Hence, data validation from SVM converges with the experimental observations that BiFeO<sub>3</sub>-WO<sub>3</sub> composites calcined at 550°C are capable of producing good degradation efficiency for MB dye with a higher rate constant when compared to that of BiFeO<sub>3</sub>-WO<sub>3</sub>

**Table IV** SVM-predicted data for MB degradation pseudo first-order kinetics and degradation efficiency for the BiFeO<sub>3</sub>-WO<sub>3</sub> nanocomposites calcined at 550°C and 650°C

S. No.	Sample code	Temperature (°C)	Predicted pseudo first-order kinetics			Predicted MB degradation efficiencies for various exposure time		
			Slope k (min <sup>-1</sup> )	Standard Error	R <sup>2</sup> value	3 h	6 h	9 h
1	BiFeO <sub>3</sub> -WO <sub>3</sub>	550	0.126(4)	0.014(5)	0.949(2)	48.9	56.4	67.6
2		650	0.083(5)	0.011(1)	0.932(5)	21.9	25.0	49.5

calcined at 650°C. The relative significance of input variables on the methylene blue dye removal efficiency is shown as a percentile score in Table V.

It has been identified that all input variables played a role in MB dye removal. However, the greatest influence was shown by dye concentration, which primarily determined the effluent removal rate. The analysis of the SVM model has shown that the methylene blue dye can be degraded using BiFeO<sub>3</sub>-WO<sub>3</sub> nanocomposites calcined at 550°C and 650°C. Their outputs clearly demonstrated that under enriched optimum conditions such as an initial dye concentration of 10 mg/L, constant pH of 5, photocatalyst dosage (1 g/L), and contact time (9 h), BiFeO<sub>3</sub>-WO<sub>3</sub> calcined at 550°C is capable of degrading MB dye effectively. It has been found that these results are qualitatively similar to the experimental result obtained through a laboratory photocatalytic setup. If more analysis is performed through the SVM model, there exists an ample chance of improving this model in degradation experiments.

## Conclusion

In summary, BiFeO<sub>3</sub>-WO<sub>3</sub> nanocomposites have been successfully synthesized through sol-gel process at two different calcination temperatures, 550°C and 650°C. The synthesized nanocomposite powders of BiFeO<sub>3</sub>-WO<sub>3</sub> were used for XRD structural analysis, revealing that the diffraction peaks of the composite indicate both rhombohedral BiFeO<sub>3</sub> and monoclinic WO<sub>3</sub> material. It has also been found that a sample calcined at 650°C appears to exhibit higher crystallinity through the observation of high-intensity x-ray diffraction peaks and higher grain growth was observed from FE-SEM images when compared to composite powders prepared at 550°C. SEM images also suggest that the synthesized composites have different morphologies, i.e. spherical-shaped nanoparticles, indicating that the BFO particles belong to WO<sub>3</sub>. The surface morphology of BiFeO<sub>3</sub>-WO<sub>3</sub> calcined 550°C was found to have a unique surface area with less agglomeration and porosity when compared with BiFeO<sub>3</sub>-WO<sub>3</sub> prepared at 650°C. Upon increasing the calcination temperature from 550°C to 650°C, a reduction in the band gap energy was noticed for the title composites. FT-IR measurement confirmed the vibrational structure of composite and evidenced IR absorptions due to Bi-O, Fe-O, and W-O at 400–700 cm<sup>-1</sup> which substantiates

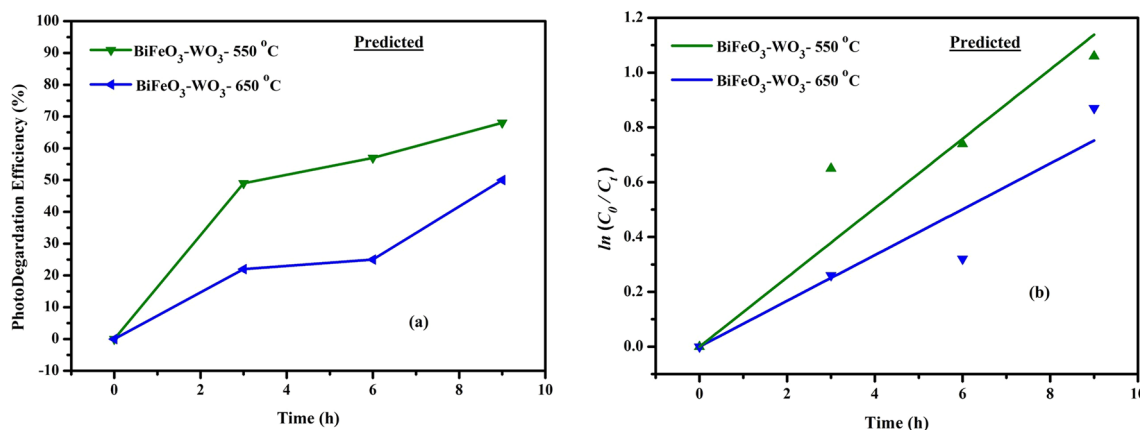


**Fig. 8** (a) Predicted plots through SVM model photodegradation efficiencies versus time and (b) Exposure time versus  $\ln(C_0/C_t)$  for BFO-WO<sub>3</sub> nanocomposites calcined at 550°C and 650°C

**Table V** Relative importance (%) of input variables on methylene blue (MB) dye removal efficiency

S. No.	Operational (Input) variables	Importance range (%)
1	Irradiation time (h)	10
2	Concentration of methylene blue (mg/L)	45
3	Photocatalyst dosage (mg/L)	40
4	pH of the medium	5

the formation of BiFeO<sub>3</sub>-WO<sub>3</sub> nanocomposite. Photocatalytic dye degradation measurements revealed that the BiFeO<sub>3</sub>-WO<sub>3</sub> nanocomposites calcined at 550°C exhibited better degradation ability for degrading methylene blue dye than that of the sample calcined at 650°C. These results confirmed that MB degradation efficiency depends not only on the optical absorption and band gap energy but is also influenced by the calcination temperature, surface morphology and crystallite size. Since the surface morphology and crystallite sizes of photocatalysts played a crucial role in generating ·O<sub>2</sub><sup>-</sup> and ·OH species, effective removal of MB dye for the BiFeO<sub>3</sub>-WO<sub>3</sub> sample calcined at 550°C is more pronounced. The intelligent SVM model has been utilized to validate the experimental degradation data of methylene blue and its predictions were found to be in good agreement with experimental data. The convergence of experimental and theoretical data on photocatalytic MB dye degradation activity of BiFeO<sub>3</sub>-WO<sub>3</sub> indicated the reliability of the obtained results.

**Acknowledgments** One of the authors, Dr. G.Ramesh Kumar, wishes to acknowledge all his collaborators for their kind research and moral support to bring this work to the level of publication.

**Conflict of interest** The authors declare that they have no conflict of interest.

## References

1. S.K. Marttinen, R.H. Kettunen, and J.A. Rintala, Occurrence and removal of organic pollutants in sewages and landfill leachates. *Sci. Total Environ.* 301, 1–12 (2003).
2. K. Pazdzior, L. Bilinska, and S. Ledakowicz, A review of the existing and emerging technologies in the combination of AOPs and biological processes in industrial textile wastewater treatment. *Chem. Eng. J.* 376, 120597 (2019).
3. Q. Ke, Y. Zhang, X. Wu, X. Su, Y. Wang, H. Lin, R. Mei, M.Z. Yu Zhang, C. Hashmi, and J.C. Chen, Sustainable biodegradation of phenol by immobilized *Bacillus* sp SAS19 with porous carbonaceous gels as carriers. *J. Environ. Manage* 222, 185 (2018).
4. O.S. Abu-Rizaiza, Modification of the standards of wastewater reuse in Saudi Arabia. *Water Res.* 33, 2601 (1999).
5. J.A. Faby, F. Brissaud, and J. Bontoux, Wastewater reuse in France: water quality standards and wastewater treatment technologies. *Water Sci Technol.* 40, 37 (1999).
6. G. Crini, and E. Lichtfouse, Advantages and disadvantages of techniques used for wastewater treatment. *Environ. Chem. Lett.* 17, 145 (2019).
7. F.C. Moreira, R.A.R. Boaventura, E. Brillas, and V.J.P. Vilar, Electrochemical advanced oxidation processes: a review on their application to synthetic and real wastewaters. *Appl. Catal. B Environ.* 202, 217 (2017).
8. E. Manoli, and C. Samara, The removal of polycyclic aromatic hydrocarbons in the wastewater treatment process: experimental calculations and model predictions. *Environ. Pollut.* 151, 477 (2008).
9. M. Mehrjouei, S. Müller, and D. Möller, A review on photocatalytic ozonation used for the treatment of water and wastewater. *Chem. Eng. J.* 263, 209 (2015).
10. L.G.C. Villegas, N. Mashhadi, M. Chen, D. Mukherjee, K.E. Taylor, and N. Biswas, A short review of techniques for phenol removal from wastewater. *Curr. Pollut. Rep.* 2, 157 (2016).
11. A. Fujishima, and K. Honda, Electrochemical photolysis of water at a semiconductor electrode. *Nature* 238, 37–38 (1972).
12. N. Daneshvar, M.H. Rasoulifard, A.R. Khataee, and F. Hosseinzadeh, Removal of C.I. acid orange 7 from aqueous solution by UV irradiation in the presence of ZnO nanopowder. *J. Hazard. Mater.* 143, 95–101 (2007).
13. A. Dandia, P. Saini, R. Sharma, and V. Parewa, Visible light driven perovskite-based photocatalysts: a new candidate for green organic synthesis by photochemical protocol. *Curr. Opin. Green Sustain. Chem.* 3, 100031 (2020).

14. S. Irfan, Z. Zhuanghao, F. Li, Y.X. Chen, G.X. Liang, J.T. Luo, and F. Ping, Critical review: Bismuth ferrite as an emerging visible light active nanostructured photocatalyst. *J. Mater. Res. Technol.* 8, 6375 (2019).
15. Y. Huo, M. Miao, Y. Zhang, J. Zhu, and H. Li, Aerosol-spraying preparation of a mesoporous hollow spherical BiFeO<sub>3</sub> visible photocatalyst with enhanced activity and durability. *Chem. Commun.* 47, 2089 (2011).
16. J. Jiang, J. Zou, M.N. Anjum, J. Yan, L. Huang, Y. Zhang, and J. Chen, Synthesis and characterization of wafer-like BiFeO<sub>3</sub> with efficient catalytic activity. *Solid State Sci.* 13, 1779 (2011).
17. Y. Subramanian, B. Mishra, S. Mandal, R. Gubendiran, and Y.S. Chaudhary, Design of heterostructured perovskites for enhanced photocatalytic activity: insight into their charge carrier dynamics. *Mater. Today: Proc.* 35, 179 (2021).
18. Y. Ma, P. Lv, F. Duan, J. Sheng, S. Lu, H. Zhu, M. Du, and M. Chen, Direct Z-scheme Bi<sub>2</sub>S<sub>3</sub>/BiFeO<sub>3</sub> heterojunction nanofibers with enhanced photocatalytic activity. *J. Alloys Comp.* 834, 155158 (2020).
19. D.P. DePuccio, P. Botella, B. O'Rourke, and C.C. Landry, Degradation of methylene blue using porous WO<sub>3</sub>, SiO<sub>2</sub>-WO<sub>3</sub>, and their Au-loaded analogs: adsorption and photocatalytic studies. *ACS Appl. Mater. Interf.* 7, 1987 (2015).
20. X. Liu, H. Zhai, P. Wang, Q. Zhang, Z. Wang, Y. Liu, Y. Dai, B. Huang, X. Qin, and X. Zhang, Synthesis of a WO<sub>3</sub> photocatalyst with high photocatalytic activity and stability using synergetic internal Fe<sup>3+</sup> doping and superficial Pt loading for ethylene degradation under visible-light irradiation. *Catal. Sci. Technol.* 9, 652–658 (2019).
21. M.B. Tahir, G. Nabi, N.R. Khalid, and N.R. Khalid, Synthesis of nanostructured based WO<sub>3</sub> materials for photocatalytic applications. *J. Inorg. Organomet. Polym.* 28, 777 (2018).
22. J. Mioduska, A. Zielińska-Jurek, M. Janczarek, J. Hupka, The effect of calcination temperature on structure and photocatalytic properties of WO<sub>3</sub>/TiO<sub>2</sub> nanocomposites. *J. Nanomaterials.* 3145912 (2016).
23. Y. Subramanian, B. Mishra, P.M. Rajashree, N. Kumar et al., Efficient degradation of endocrine-disrupting compounds by heterostructured perovskite photocatalysts and its correlation with their ferroelectricity. *New J. Chem.* 46, 11851 (2022).
24. N.M. Mahmoodi, J. Abdi, M. Taghizadeh, A. Taghizadeh, B. Hayati, A.A. Shekarchi, and M. Vossoughi, Activated carbon/metal-organic framework nanocomposite: preparation and photocatalytic dye degradation mathematical modeling from wastewater by least squares support vector machine. *J. Environ. Manag.* 233, 660 (2019).
25. M. Ateia, M.G. Alalm, D. Awfa, M.S. Johnson, and C. Yoshimura, Modeling the degradation and disinfection of water pollutants by photocatalysts and composites: a critical review. *Sci. Total Environ.* 698, 134197 (2019).
26. M.A.S. VaezZarringhalam MoghaddamAlijani, Optimization and modeling of photocatalytic degradation of Azo dye using a response surface methodology (RSM) Based on the central composite design with immobilized titania nanoparticles. *Indus. Eng. Chem. Res.* 51, 4199 (2012).
27. Y. Subramanian, V. Ramasamy, R.K. Gubendiran, G.R. Srinivasan, and D. Arulmozhi, Structural, optical, thermal and photocatalytic dye degradation properties of BiFeO<sub>3</sub>-WO<sub>3</sub> Nanocomposites. *J. Electron. Mater.* 47, 7212 (2018).
28. H. Heryanto, B. Abdullah, and D. Tahir, Analysis of structural properties of X-ray diffraction for composite copper-activated carbon by modified Williamson-Hall and size-strain plotting methods. *J. Phys: Confer. Series.* 1080, 012007 (2018).
29. J. Cai, W. Xin, G. Liu, D. Lin, and D. Zhu, Effect of calcination temperature on structural properties and photocatalytic activity of Mn-C-codoped TiO<sub>2</sub>. *Mater. Res.* 19, 401 (2016).
30. R. Ghosh, K.S. Asha, S.M. Pratik, A. Datta, R. Nath, and S. Mandal, Synthesis, structure, photocatalytic and magnetic properties of an oxo-bridged copper dimer. *RSC Adv.* 4, 21195 (2014).
31. U. OparaKrasovec, A.S. ŹurcaVuk, and B. Orel, IR Spectroscopic studies of charged–discharged crystalline WO<sub>3</sub> films. *Electrochim. Acta* 13, 1921 (2001).
32. T. Gao, Z. Chen, Y. Zhu, F. Niu, Q. Huang, L. Qin, X. Sun, and Y. Huang, Synthesis of BiFeO<sub>3</sub> nanoparticles for the visible-light induced photocatalytic property. *Mater. Res. Bull.* 59, 6 (2014).
33. S. Alkaykh, A. Mbarek, and E.E. Ali-Shattle, Photocatalytic degradation of methylene blue dye in aqueous solution by MnTiO<sub>3</sub> nanoparticles under sunlight irradiation. *Heliyon.* 6, e03663 (2020).
34. Y. Subramanian, V. Ramasamy, R. Karthikeyan, G. Srinivasan, D. Arulmozhi, R. Gubendiran, and M. Sriramalu, Investigations on the enhanced dye degradation activity of heterogeneous BiFeO<sub>3</sub>-GdFeO<sub>3</sub> nanocomposite photocatalyst. *Heliyon* 5, e01831 (2019).
35. R. Cheng, L. Shen, J. Yu, S. Xiang, and X. Zheng, Photocatalytic inactivation of bacteriophage f2 with Ag<sub>3</sub>PO<sub>4</sub>/g-C<sub>3</sub>N<sub>4</sub> composite under visible light irradiation: performance and mechanism. *Catalysts* 8, 406 (2018).
36. H. Yang, A short review on heterojunction photocatalysts: Carrier transfer behavior and photocatalytic mechanisms. *Mater. Res. Bull.* 142, 111406 (2021).
37. T. Cheng, H. Gao, G. Liu, Z. Pu, S. Wang, Z. Yi, X. Wu, and H. Yang, Preparation of core-shell heterojunction photocatalysts by coating CdS nanoparticles onto Bi<sub>4</sub>Ti<sub>3</sub>O<sub>12</sub> hierarchical microspheres and their photocatalytic removal of organic pollutants and Cr(VI) ions. *Colloids Surf., A* 633, 127918 (2022).
38. Y. Gu, B. Guo, Z. Yi, X. Wu, J. Zhang, and H. Yang, Morphology modulation of hollow-shell ZnSn(OH)<sub>6</sub> for enhanced photodegradation of methylene blue. *Colloids Surf., A* 653, 129908 (2022).
39. M.S. Mazloom, F. Rezaei, A. Hemmati-Sarapardeh, M.M. Husein, S. Zendejboudi, and A. Bemani, Artificial intelligence based methods for asphaltene adsorption by nanocomposites: application of group method of data handling, least squares support vector machine, and artificial neural networks. *Nanomaterials* 10, 890 (2020).
40. Y. Subramanian, R. Veena, S. Muhammed Ali, A. Kumar, R. Gubendiran, A. Dhanasekaran, D. Gurusamy, and K. Muniandi, Artificial intelligence technique based performance estimation of solid oxide fuel cells. *Mater. Today: Proc.* (2021). <https://doi.org/10.1016/j.matpr.2021.06.412>.
41. T.A. Oyehan, M.A. Liadi, and I.O. Alade, Modeling the efficiency of TiO<sub>2</sub> photocatalytic degradation of MTBE in contaminated water: a support vector regression approach. *SN Appl. Sci.* 1, 386 (2019).
42. T. Zhang, C. Wu, Z. Xing, J. Zhang, S. Wang, X. Feng, J. Zhu, X. Lu, and L. Mu, machine learning prediction of photocatalytic lignin cleavage of C-C bonds based on density functional theory. *Mater. Today Sustain.* 20, 100256 (2022).

**Publisher's Note** Springer Nature remains neutral with regard to jurisdictional claims in published maps and institutional affiliations.

Springer Nature or its licensor (e.g. a society or other partner) holds exclusive rights to this article under a publishing agreement with the author(s) or other rightsholder(s); author self-archiving of the accepted manuscript version of this article is solely governed by the terms of such publishing agreement and applicable law.